ACS Sustainable Chemistry & Engineering
Research Article
pubs.acs.org/journal/ascecg

Hydrogen Generation of Cu_2O Nanoparticles/MnO−MnO_2 Nanorods Heterojunction Supported on Sonochemical-Assisted Synthesized Few-Layer Graphene in Water-Splitting Photocathode

Yen-Hsun Su,* Shi-Hong Huang, Po-Yen Kung, Tin-Wei Shen, and Wen-Lin Wang

Department of Materials Science and Engineering, National Cheng Kung University, No. 1, University Rd., East District, 70101 Tainan City, Taiwan

Supporting Information

ABSTRACT: In this study, we investigated the production of hydrogen by photochemical water splitting. A multi-shaped Cu_2O nanoparticles/MnO−MnO_2 nanorods heterojunction on a few-layer graphene-based electrode serves as the photocathode. Multi-shaped Cu_2O nanoparticles, including truncated cubic shape, cuboctahedral shape, truncated octahedral shape, and octahedral shape, were then coated on square manganese nanorods on a few-layer graphene-based electrode as the photosensitizer. Finally, the efficiency of hydrogen production was measured and recorded. The Cu_2O nanoparticles/MnO−MnO_2 nanorods heterojunction generates photoelectrons to reduce hydrogen ions into hydrogen gas. The manganese dioxide nanorods were combined with cuprous oxide multi-shaped nanoparticles to be simultaneously utilized in hydrogen production as a photochemical water-splitting solar cell. The highest rate of hydrogen generation is 33.0 mL/min m^2 under solar simulation radiation. This study highlights the significance of a back electron−hole recombination loss and transportation process on the surface of a water-splitting photocathode, retarding the appearance of the photocurrent and requiring a greater amount of energy from a solar device.

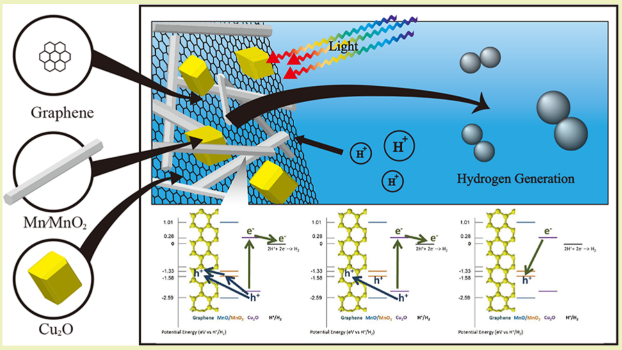

KEYWORDS: *Water splitting, Photocathode, Back electron−hole recombination loss, Cuprous oxide, Graphene, Manganosite*

INTRODUCTION

Graphene is an allotrope of carbon whose structure is a single planar sheet of sp2-bonded carbon atoms, which are densely packed in a honeycomb crystal lattice.[1] High quality graphene is very strong, light, nearly transparent, and an excellent conductor of heat and electricity. Graphene has a remarkably high electron mobility at room temperature, with reported values[1] in excess of 15,000 cm^2 V^{-1} s^{-1}. The corresponding resistivity of the graphene sheet would be 10^{-6} Ω cm.[2,3] This is less than the resistivity of silver, making graphene the substance of lowest resistivity known at room temperature. This material only absorbs 2.3% of visible light; it is a candidate for applications as a highly conductive and transparent electrode[4] in areas of supercapacitance. Few-layer graphene also has excellent performances in industrially scalable electric devices.[5]

Manganosite is usually used in supercapacitance due to its many oxides states. Manganosite consists of Mn^{2+} and O^{2-} molecules forming an octahedral geometry and a cubic crystal structure.[6] Currently, some of the most common methods to make manganese oxide compounds involve hydrothermal synthesis where $MnSO_4{\cdot}H_2O$, $KMnO_4$, and $MnSO_4$ are mixed together under high pressure allowing the precipitate to form.[7,8] It has potential for use in hybrid energy storage devices due to its quasi-reversible electron transfer that provides high pseudocapacitative energy density.[9] Within the past decade, there has been an increased effort in the development of new hybrid energy storage devices that possess both high energy and high power density, which are beneficial for creating more energy efficient storage and delivery.[10] Such systems will find use in hybrid electric vehicles, mobile electronic devices, memory back-up systems, and industrial equipment that rely on long cycle-life times and an uninterruptable power supply.[10−13] Asymmetric supercapacitors are promising hybrid energy storage devices as they are able to provide a wider operating voltage at higher energy compared to symmetric capacitors.[14] Such supercapacitors are comprised of an anode that is usually an activated carbon, while the cathode is generally a composite consisting of a carbon material and transition metal oxide; these materials are considered promising due to their availability, cost effectiveness, and environmentally friendly nature. Asymmetric supercapacitors make use of the different potential windows in the anode and cathode leading to an increased operational voltage of the aqueous electrolyte in the cell, meaning that interfacial capacitance, energy, and power density are maximized.[14] The

Received: February 25, 2015
Published: July 15, 2015

high pseudocapacitative energy density manganosite materials with long lifetimes can possibly convert storage energy density into chemical energy of hydrogen generation by photochemical water splitting. However, few papers report this application.

Many heterogeneous photocatalysts have semiconductor properties. When the energy of incident light is larger than that of a band gap, electrons and holes are generated in the conduction band and valence band, respectively. The photogenerated electrons and holes cause redox reactions similarly to electrolysis.[15−18] Cuprous oxide (Cu_2O) is a p-type semiconductor with a direct band gap of 2.17 eV.[19] Cu_2O nanostructures have been demonstrated to be useful for photoactivated water splitting into H_2 and O_2.[20,21]

In this study, a multi-shaped Cu_2O nanoparticles/MnO−MnO_2 nanorods heterojunction on a few-layer graphene-based electrode serves as the photocathode. Cu_2O/MnO−MnO_2 has big issues with photocorrosion. Therefore, in this research, Cu_2O/MnO−MnO_2 is utilized as the cathode to prevent corrosion. Multi-shaped Cu_2O nanoparticles, including truncated cubic shape, cuboctahedral shape, truncated octahedral shape, and octahedral shape, were then coated on square manganese nanorods as the photosensitizer. A manganese oxide can be reductive hydrogen, but manganese dioxide cannot reduce hydrogen. Manganese oxide cannot absorb visible light, but manganese dioxide absorbs visible light due to its energy band gaps. The photochemical water-splitting scheme of a Cu_2O nanoparticles/MnO−MnO_2 nanorods heterojunction under AM 1.5 G radiation is shown in Figure 1. After absorbing photons by Cu_2O nanoparticles, excited electrons jump from the valence band to conduction band and then reduces protons into hydrogen gas. The valence band of MnO is higher than that of Cu_2O, which prevents the excited electrons from transferring into cathodes. The electronic hole transfers from the valence band of Cu_2O nanoparticles to that of MnO_2 and then transfers into a cathode. The chemical potential of the excited electron is enough to reduce hydrogen ion into hydrogen gas, as the shown in Figure 1. But the chemical potential of electronic hole is not enough to oxide the OH^- into oxygen gas. Therefore, the bias voltage is applied to the anode in order to increase the chemical potential of the electronic hole to oxide the OH^- into oxygen gas. The achieved results offer very useful guidelines in designing photocathodes for high-efficiency, low-cost, and flexible photoelectrochemical cells by using cheap, earth-abundant materials for clean solar hydrogen generation at large scales.

■ EXPERIMENTAL SECTION

Few-Layer Graphene Preparation. Graphite was dispersed in the isopropanol solvent (cylindrical vial, 10−25 mL solvent) at a concentration of 0.1 mg/mL by sonicating in a sonic bath for 30 min. The resultant dispersion was placed in a centrifuge (CF) for 90 min at 4000 rpm. Sediment was dispersed again in 16 mL of isopropanol by bath sonication for 30 min. The sample was then centrifuged for 90 min at 500 rpm. Finally, the supernatant was collected. Reduced graphene oxide (rGO) and exfoliated graphene oxide (GO) are the hydrophilic materials.[22] Graphene is a hydrophobic material. Either the hydrophilic material or hydrophobic material is well dispersed into isopropanol. The solubility of graphene into isopropanol is as high as 0.5 mg/mL.[23]

MnO Preparation. Potassium permanganate ($KMnO_4$) and manganese sulfate ($MnSO_4$) were prepared by dissolving in deionized water as 0.1 and 0.6 M. Twenty milliliters of a $KMnO_4$ solution and 20 mL of a $MnSO_4$ solution were mixed while stirring. The hydrothermal synthesis was carried out at 140 °C for 12 h. After the reaction was completed, the experimental temperature decreased to room temperature, and the black product was washed with deionized water and ethanol and then dried at 60 °C for 24 h.

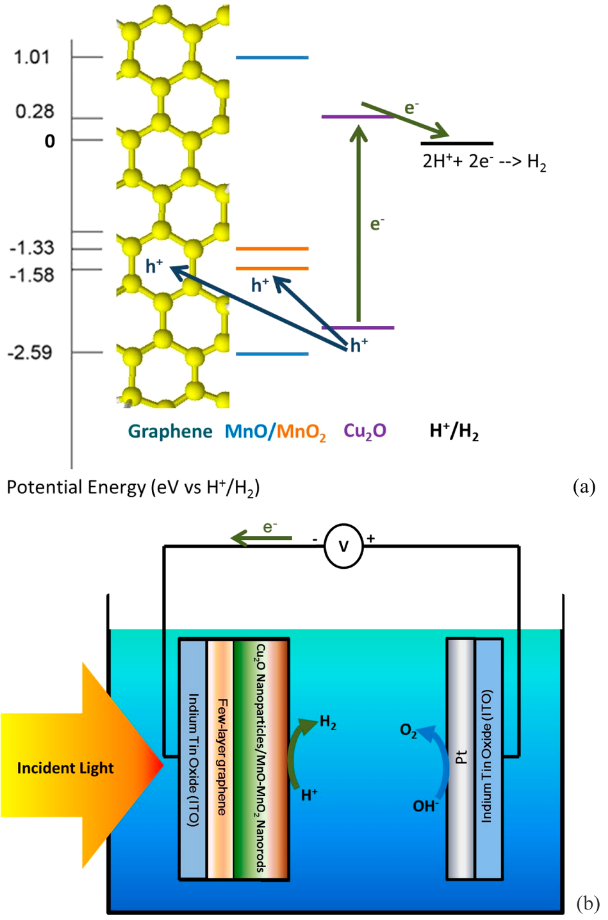

Figure 1. Photochemical water-splitting scheme of (a) electronic structure of Cu_2O nanoparticles/MnO−MnO_2 nanorods heterojunction and (b) photovoltagic cell of watering splitting under AM 1.5 G radiation.

Cu_2O Preparation. For the syntheses of Cu_2O nanocrystals with different product morphologies, 9.4, 9.2, 9.0, and 8.8 mL of deionized water were respectively added to four sample bottles labeled A, B, C, and D. Then, 0.1 mL of 0.1 M $CuCl_2$ solution and 0.087 g of SDS powder were added to each bottle with vigorous stirring until dissolution of the powder, and the resulting solutions were allowed to stand for 5 min. Next, 0.25, 0.45, 0.65, and 0.85 mL of 0.2 M $NH_2OH{\cdot}HCl$ were mixed with the solutions in bottles A, B, C, and D, respectively. After the solutions were shaken for 10 s, 0.25 mL of 1.0 M NaOH was added, and the bottles were shaken for an additional 10 s. The total solution volume in each bottle is 10 mL. We aged the solutions for 2 h to obtain the desired Cu_2O nanocrystal products. After aging, the four samples were centrifuged at 5000 rpm for 5 min.

Electrodes Preparation. The Cu_2O/MnO−MnO_2 nanorods/few-layer graphene composites of the photocathode are prepared as the follows. Ten milligrams of few-layered graphene dispersed in the isopropanol solvent was evaporated on the 3 cm × 1 cm clean ITO glass substance. A total of 9.5

mg of MnO−MnO_2 nanorods is mixed with 0.5 wt % polytetrafluoroethylene (PTEF) and then coated on the 3 cm × 1 cm ITO glass substance modified by few-layer graphene. Then, the samples are dried at 80 °C for 24 h. Cu_2O nanocrystal solutions were dip-coated on the MnO−MnO_2 nanorods/few-layer graphene/ITO glass substance. The Cu_2O/MnO−MnO_2 nanorods/few-layer graphene composites of the photocathode are prepared. A total of 3 mL/cm^2 of 10^{-3} M H_2PtCl_6 in isopropyl alcohol was dropped onto ITO glasses at 350 °C for 12 h to prepare the anode.

Measurement. Scanning electron microscopy (SEM) showed the morphology of MnO and Cu_2O. X-ray diffraction (XRD) was employed in order to understand the crystallinity of the few-layer graphene and MnO and Cu_2O structure. An energy dispersive spectrometer (EDS) detected the elements of productions. The optical absorbance measurement was obtained with the ultraviolet−visible (UV−vis) spectrometer. Electrochemical instrumentation measured the electric properties, current, and voltages. The power of the simulated solar energy (AM 1.5 G) was found to be 100 mW cm^{-2}, and the power of filtered light was calibrated by an optical power meter and a silicon photodiode (PV Measurements, Inc.). The photovoltagic cell of watering splitting is a device with two electrodes, as shown in Figure 1b. In the measurement of the photocurrent, the electric instrument (Keithly 2400) was employed to measure the current under the AM 1.5 G radiation. Hydrogen generation rate was measured by gas chromatography (ChromTech).

RESULTS AND DISCUSSION

Raman spectroscopy is a fast and nondestructive method for the characterization of carbon structures, which is a powerful tool for evaluating the extent of exfoliation in graphite. In Figure 2, the G band for exfoliated graphene, due to the presence of sp^2-hybridized carbon atoms, remains virtually unchanged relative to that of intact graphite (i.e., 1582 cm^{-1}), thus suggesting the absence of doping (p- or n-type) on exfoliated graphene, signifying the lack of appreciable electronic interactions between the solvents used and graphite. In other words, the exfoliation of graphite by ultrasonication in isopropanol is only a physical process, taking place without the interference of electronic interactions from the solvents, then focusing in the 2D band, where its shape and position are characteristic of the exfoliated graphene layers. In a typical Raman spectrum of graphene,[24,25] the symmetric E2g mode at the Γ-point is the G mode, which is observed at approximately 1583 cm^{-1}. The D mode is a disorder-activated Raman mode with the TO phonons branch near the K-point, which is observed at approximately 1350 cm^{-1}. The 2D mode at 2680 cm^{-1} is the second-order Raman scattering involving TO phonons near the K-point. Raman spectra of few-layer graphene is also similar to graphite,[26] except for the 2D band.[27] Highly oriented pyrolytic graphite (HOPG) and few-layer grahene have two peaks and more than three peaks around 2680 cm^{-1} in the Raman spectrum, respectively, which distinguish the 2D band for HOPG from that for few-layer graphene.[27] Figure 2 presents Raman spectra of exfoliated graphene. There are three peaks around 2680 cm^{-1}, which determine that the exfoliated graphene is a few-layer graphene. According to transmission electronic microscopic observations in Figure 2b, the exfoliated graphene is few-layer graphene, which corresponds to the results from the Raman spectrum.

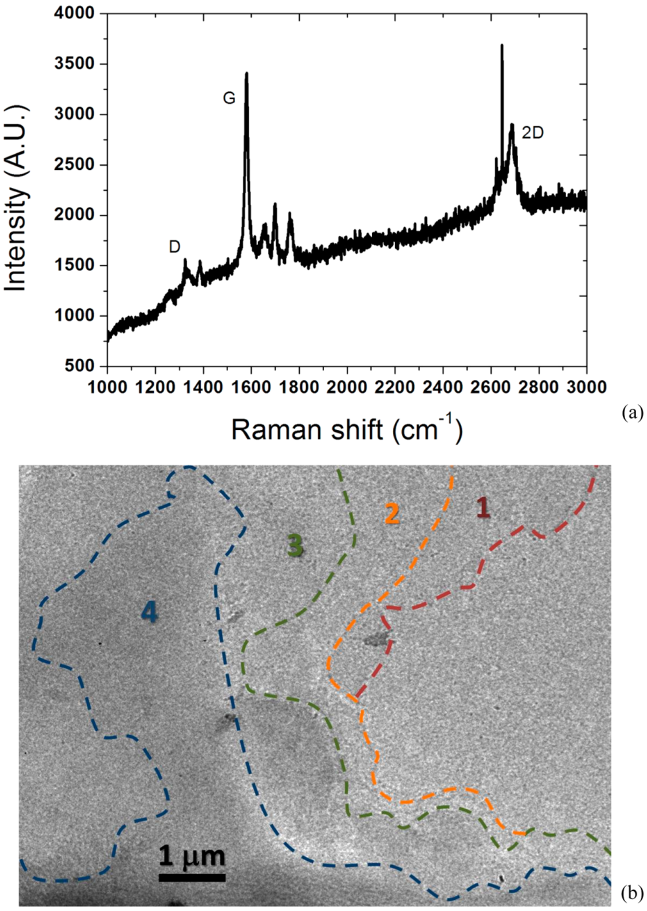

Figure 2. (a) Raman spectra and (b) morphology of exfoliated few-layer graphene, as obtained by ultrasonication in isopropanol solvent.

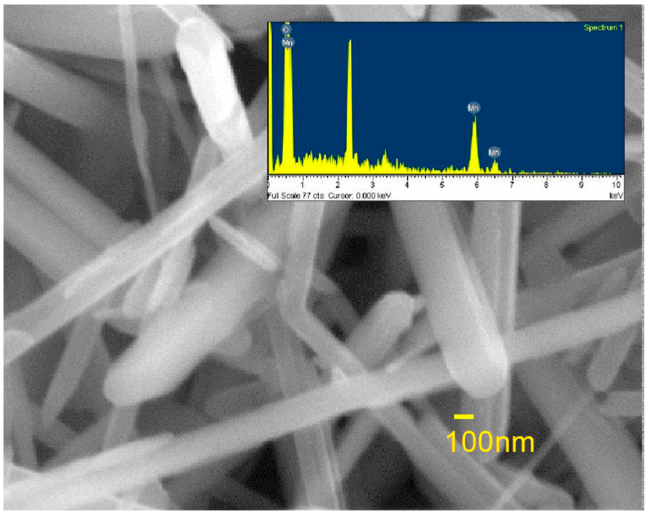

Figure 3. Morphology of the MnO_2 nanorods. Insets show EDS of manganese and oxide elements views of the particle.

Morphology and element analysis of the MnO nanostructures are shown in Figure 3. The MnO shape is a nanorod. Morphologies of the Cu_2O nanocrystals with different synthesis parameters are presented in Figure 4. Different particle morphologies can be clearly distinguished in these samples. Table 1 lists the average particle sizes and standard deviations for the four samples obtained from their size distribution. Cu_2O

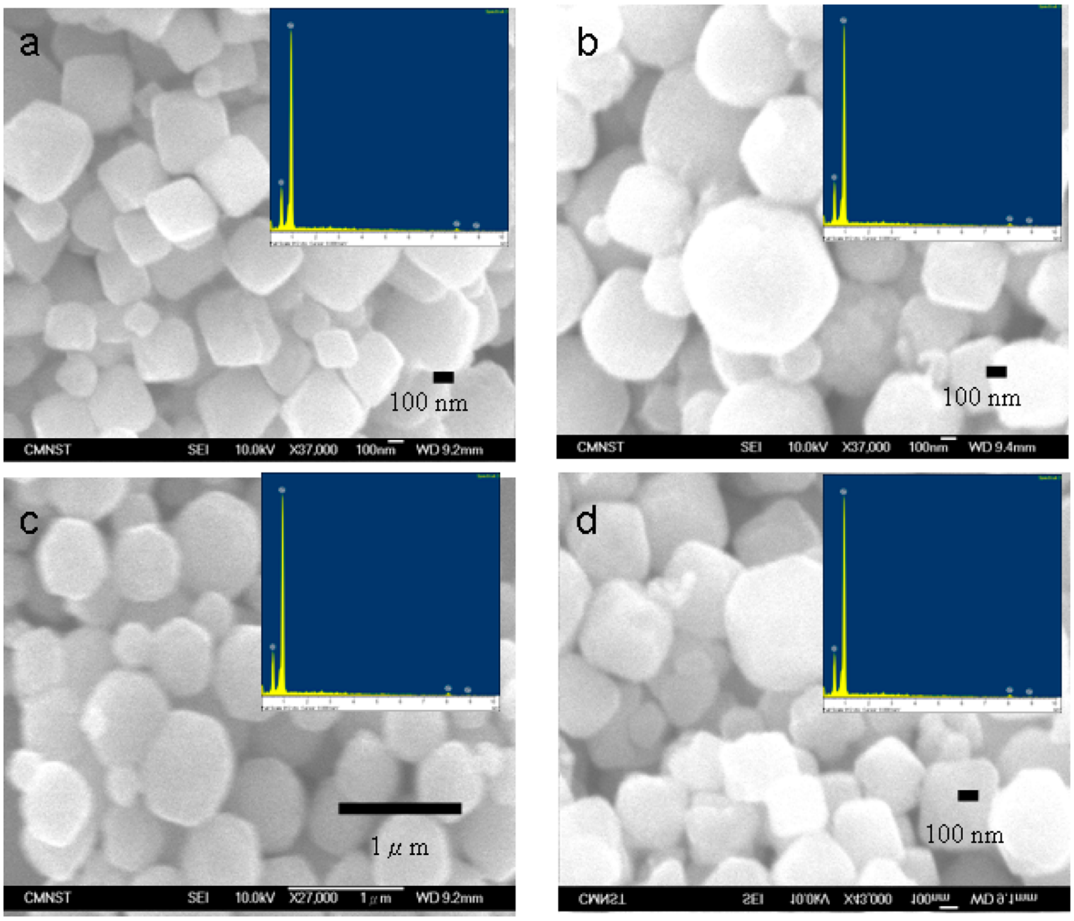

Figure 4. Morphologies of the Cu_2O nanocrystals synthesized in sample bottles A, B, C, and D with increasing amounts of $NH_2OH{\cdot}HCl$ added to the solutions in the bottles. The particle morphologies are (a) truncated cubic, (b) cuboctahedral, (c) truncated octahedral, and (d) octahedral in shape. Insets show EDS of iron cuprous/oxide views of individual nanocrystals.

Table 1. Average Particle Sizes and Standard Deviations of Cu_2O Nanocrystals Synthesized in Samples A−D (truncated cubic shape, cuboctahedral shape, truncated octahedral shape, and octahedral shape)

sample	morphology	average particle size (nm)
A	truncated cubic	288.33 ± 80.66
B	cuboctahedral	440.00 ± 171.60
C	truncated octahedral	602.78 ± 205.86
D	octahedral	323.33 ± 123.01

sizes have increased to 200−400 nm of truncated cubic, cuboctahedral, truncated octahedral, and octahedral structures. The nanocrystal morphologies are the same as before with truncated cubic, cuboctahedral, truncated octahedral, and octahedral structures for the respective samples, as shown in Figure 4. The surfactant SDS and the amount of $NH_2OH{\cdot}HCl$ present in the solution play a crucial role in directing the overall morphology of these intermediate structures. The amount of $NH_2OH{\cdot}HCl$ may influence the growth rate of the [111] direction and results in the formation of intermediate structures with roughly cubic, cuboctahedral, and octahedral structures. The role of SDS in assisting the cubic and octahedral nanocrystal formation was verified by replacing SDS with the same mole number of cetyltrimethylammonium bromide (CTAB) surfactant, and according to SEM observations, we found that the SDS surfactant controls the nanocrystal morphology precisely. According to energy dispersive spectroscopy (EDS) (insets, Figure 4), the nanocrystal was composed of Cu and O elements.

The crystal structures of graphene, manganosite, and manganosite/few-layer graphene composites were identified using X-ray diffraction as shown in Figure 5. Figure 5a shows the peaks for graphene at 25.48° from the graphene (JCPDS 01-0646). The 2θ peaks of MnO are marked and shown in Figure 5b, which corresponds to manganosite type MnO from MnO (JCPDS 75-1090). The other 2θ peaks are the diffection plane of α-MnO_2, which corresponds α-MnO_2 (JCPDS 44-0141). Figure 5c was compared with Figure 5b. Figure 5c was deteriorated crystallization when the MnO−MnO_2 rods modify the few-layer graphene, which also corresponds to MnO (JCPDS 75-1090) and α-MnO_2 (JCPDS 44-0141).

The syntheses of Cu_2O nanocrystals with systematic shape evolution from cubic to octahedral structures were achieved by simply varying the amount of reductant $NH_2OH{\cdot}HCl$ added to the reaction mixture. Because the reduction rate is not the same, ions will increase the collision chances that accelerate the reduction rate. The faster reduction causes ions to precipitate. The copper atoms change greatly. Precipitation would increase nucleation and growth, so the nucleation and growth rate will affect the shape of cuprous oxide. In Figure 6, the XRD patterns for the four samples are presented. The XRD patterns show the expected (110), (111), (200), (220), (311), and (222) diffraction peaks of Cu_2O and confirm that these lattice

DOI: 10.1021/acssuschemeng.5b00579
ACS Sustainable Chem. Eng. 2015, 3, 1965−1973

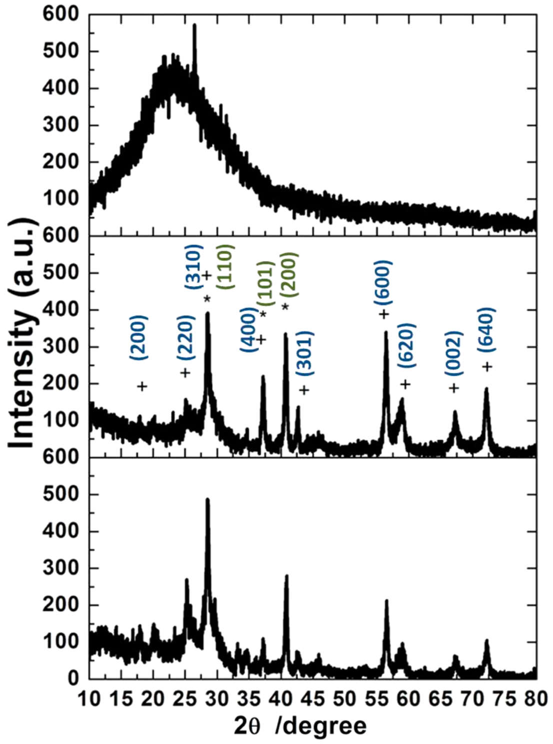

Figure 5. XRD spectra of few-layer graphene, manganese dioxide nanorods, and few-layer graphene/manganese dioxide nanorods. Upper panel is graphene, middle panel is manganese dioxide nanorods, and bottom panel is few-layer graphene/manganese dioxide nanorods (blue words and + are MnO_2; green words and ∗ are MnO).

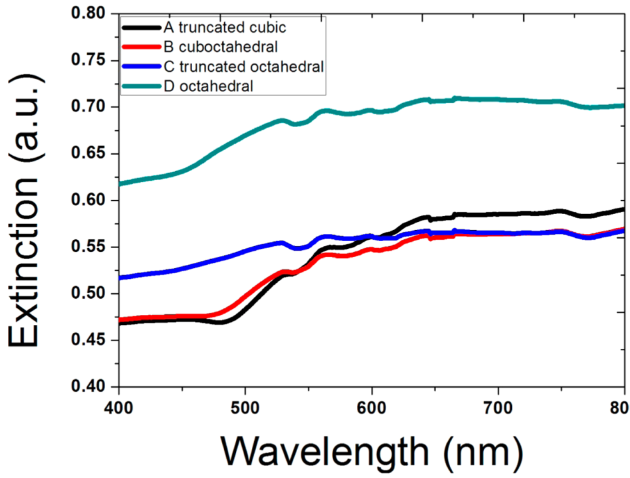

Figure 7. UV−vis absorption spectra of the Cu_2O nanocrystals in samples A−D (black line, truncated cubic; red line, cuboctahedral; blue line, truncated octahedral; green line, octahedral).

structures have a cubic crystal structure of Cu_2O. The ratios of the intensity of the (200) peak to that of the (111) peak are progressively lowered from truncated cubic to octahedral nanocrystals as a result of the decreasing {100} faces. A similar trend has been observed for cubes and octahedrals. This change in the intensity ratio also results from the preferential deposition of nanocubes on their {100} faces and octahedra on their {111} faces.

Figure 7 presents the UV−vis absorption spectra for truncated cubic, cuboctahedral, truncated octahedral, and octahedral structures. The absorption band of truncated cubic and cuboctahedral structures are in the 500−800 nm range. A broad absorption band of C (truncated octahedral) and D (octahedral structures) are in the 400−800 nm range. When Cu_2O is octahedral, the absorption ranges from 400 to 800 nm. According to SEM data in Figure 4, particle sizes of the Cu_2O nanocrystals are close to the wavelength of incident light, which means the particle sizes are in the subwavelength-scaled regime. The light scattering of Cu_2O nanocrystals increases as the

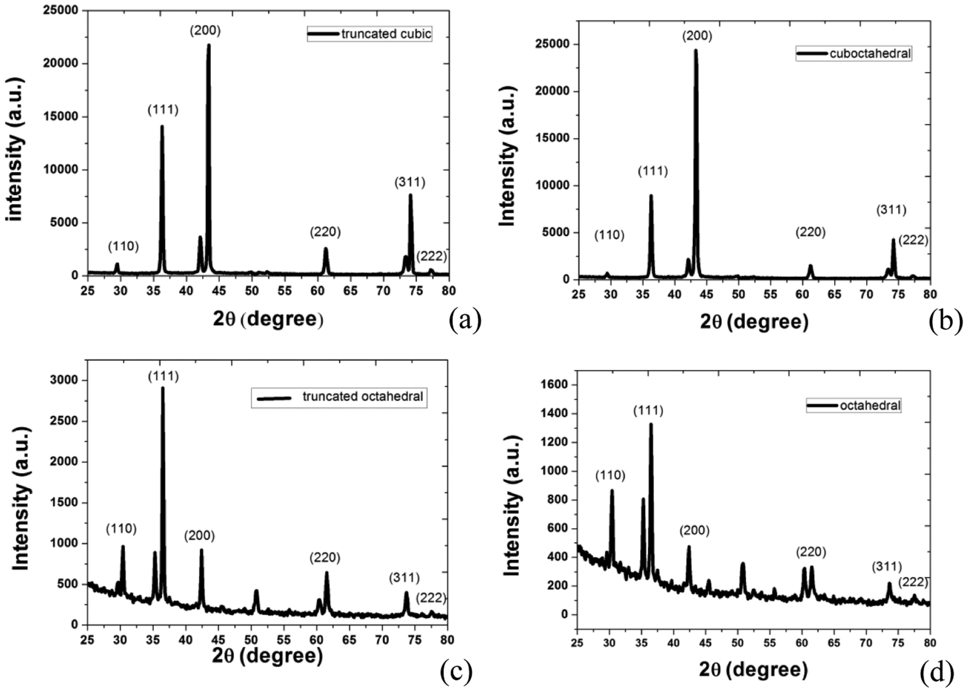

Figure 6. XRD patterns of the synthesized (a) truncated cubic, (b) cuboctahedral, (c) truncated octahedral, and (d) octahedral Cu_2O nanocrystals.

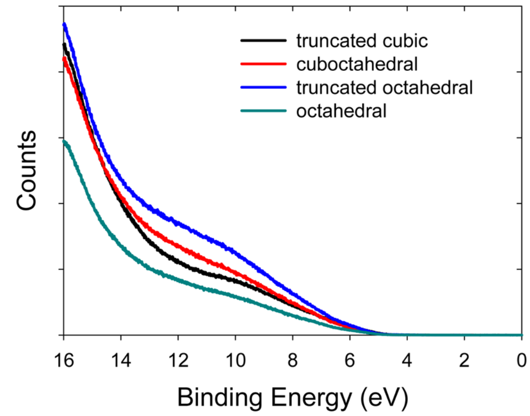

Figure 8. UPS of the Cu_2O (black line, truncated cubic; red line, cuboctahedral; blue line, truncated octahedral; green line, octahedral).

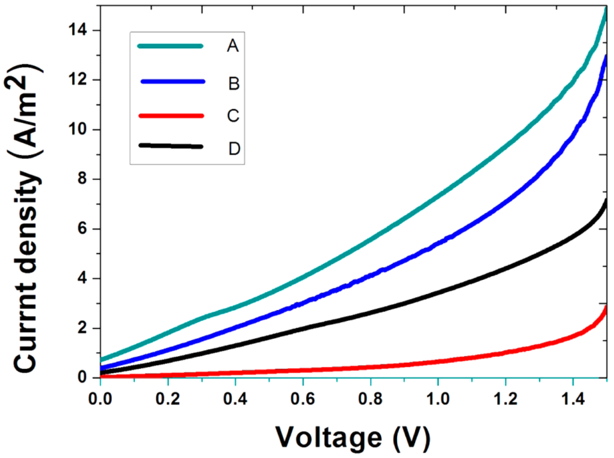

Figure 9. Photoelectric current of multi-shaped Cu_2O nanoparticles on MnO−MnO_2 nanorods supported by few-layer graphene on an ITO glass substrate as the photocathode with 0.1 M $KHCO_3$ as the electrolyte under AM 1.5 G radiation (black line, truncated cubic; red line, cuboctahedral; blue line, truncated octahedral; green line, octahedral).

Table 2. Photoelectrochemical Water-Splitting Properties of Multi-Shaped Cu_2O Nanoparticles on MnO−MnO_2 Nanorods Supported by Few-Layer Graphene on an ITO Glass Substrate as Photocathode under Simulated Solar AM 1.5 G Radiation with 0.1M $KHCO_3$ as the Electrolyte[a]

sample	$J_{\text{at 1.229}}$ (A/m^2)	$V_{\text{at }\eta\text{ max}}$ (V)	$J_{\text{at }\eta\text{ max}}$ (A/m^2)	R (mL/s m^2)	P (%)
A	9.64	0.636	4.31	0.0550	77.0
B	7.38	0.620	3.15	0.0402	77.0
C	1.08	0.624	0.38	0.0041	65.1
D	4.57	0.612	2.02	0.0258	77.1

[a] A, truncated cubic; B, cuboctahedral; C, truncated octahedral; D, octahedral. *R* is the hydrogen generation rate checked by gas chromatography. *P* is the percentage of photocurrent was from water splitting, which compares *R* with faradaic efficiency. The generated gas is collected by water displacement and determined by gas chromatography.

wavelength of incident light increases in the subwavelength-scaled regime.

Ultraviolet photoelectron spectroscopy (UPS) is utilized to determine the electronic structure close to the Fermi level.

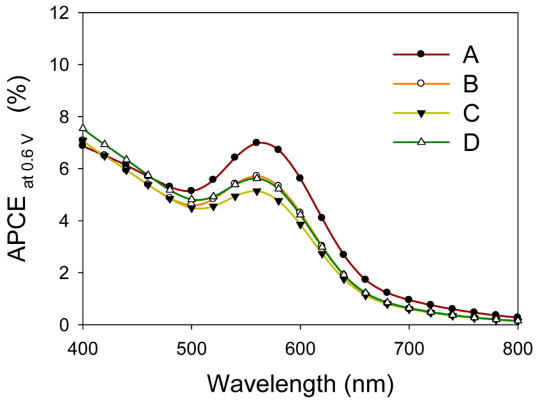

Figure 10. Absorbed photon-to-current conversion efficiency (APCE) plot of multi-shaped Cu_2O nanoparticles on MnO−MnO_2 nanorods supported by few-layer graphene on an ITO glass substrate as the photocathode with 0.1 M $KHCO_3$ as the electrolyte at 0.6 V bias voltage (A, truncated cubic; B, cuboctahedral; C, truncated octahedral; D, octahedral).

Figure 8 presents photoelectron spectroscopies of the four kinds of shapes of cuprous oxide. The electronic structures of the four kinds of shapes of cuprous oxide are similar. The tail end is close to 4.7 eV, which is corresponding to the Fermi level of p-Cu_2O.[28] The rising counts of photoelectrons above the Fermi level energy results from the Cu 3d orbital electron transition.[29] Electronic structures of the four kinds of shapes of cuprous oxide are similar, indicating that the electronic structure of the four kinds of shapes of cuprous oxide are similar. The absorption peaks are caused by the geometric effect.

The photoelectrochemical properties of multi-shaped Cu_2O on MnO−MnO_2 nanorods supported by a few-layer graphene layer on an ITO glass substrate were measured with the electrolyte of 0.1 M $KHCO_3$ under AM 1.5 G radiation, as shown in Figure 9. In this the photovoltagic cell of watering splitting, the Pt film and Cu_2O/MnO−MnO_2/Graphene/ITO are anode and cathode, respectively, as shown in Figure 1b. The electric currents are the electric properties of the photovoltagic cell with different Cu_2O nanoparticles shapes. Efficiency (η) of photoelectrochemical water splitting was evaluated according to the following equation[30,31]

$$\eta\ (\%) = \text{Jop}(1.229 - \text{Eop})/\text{Int} \times 100\%$$

Jop is the photocurrent density at Eop, Int is the intensity of incident solar light (AM 1.5 G), 1.23 V is the theoretical value for the lowest voltage able to electrolyze water into O_2 and H_2, and Eop is the applied voltage under optimal operating conditions in which the photocurrent density Jop is measured. The electric currents of multi-shaped Cu_2O on a MnO−MnO_2 nanorods with an electrolyte of 0.1 M $KHCO_3$ in the dark field are presented in Figure 1S of the Supporting Information, which is much lower than that shown with AM 1.5 G radiation in Figure 9. The efficiencies of photoelectrochemical water splitting were calculated and are presented in Table 2. The highest efficiency is the truncated cubic Cu_2O on MnO−MnO_2 nanorod as the photoelectrode. The maximum efficiency of multi-shaped Cu_2O nanoparticles on MnO−MnO_2 nanorods supported by few-layer graphene on an ITO glass substrate as the photocathode takes place close to 0.6 V bias voltage.

Absorbed photon-to-current conversion efficiency (APCE) of multi-shaped Cu_2O nanoparticles on MnO−MnO_2 nanorods

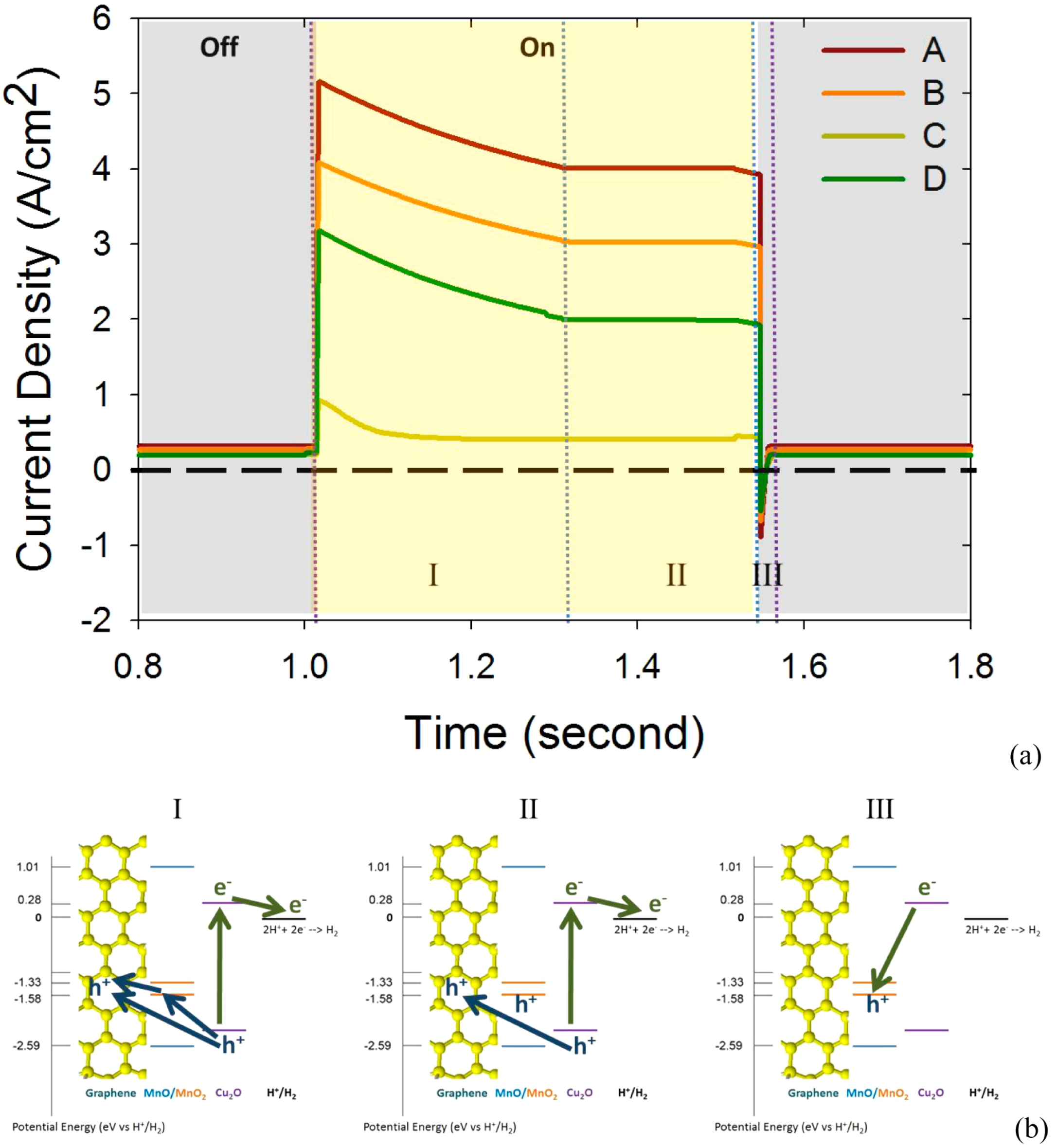

Figure 11. (a) Transient plot and (b) electron and hole transportation scheme of multi-shaped Cu_2O nanoparticles on MnO−MnO_2 nanorods supported by few-layer graphene on an ITO glass substrate as the photocathode with 0.1 M $KHCO_3$ as the electrolyte at 0.6 V bias voltage (A, truncated cubic; B, cuboctahedral; C, truncated octahedral; D, octahedral).

supported by few-layer graphene on an ITO glass substrate as the photocathode with 0.1 M $KHCO_3$ as the electrolyte at 0.6 V bias voltage is presented in Figure 10. The maximum peak of APCE is close to 560 nm, which corresponds to energy band gap of Cu_2O nanoparticles. Compared with UV−vis absorption spectra of the Cu_2O nanocrystals in Figure 7, APCE shows that light extinction due to the light scattering of Cu_2O nanocrystals geometries does not contribute to photocurrent directly. Because the light scatterings of Cu_2O nanocrystals contribute some optical loss in the UV−vis absorption data, the APCE data in Figure 10 was not totally consistent with the UV−vis absorption data. On the other hand, according to the APCE data in Figure 10, the band gap absorptions of Cu_2O nanocrystals are observed effectively. The electron in the ground state is excited to the excited state and then contributes to the photocurrent, which causes the peaks in the APCE data in Figure 10.

Transient plots of multi-shaped Cu_2O nanoparticles on MnO−MnO_2 nanorods supported by few-layer graphene on an ITO glass substrate as the photocathode with 0.1 M $KHCO_3$ as the electrolyte at 0.6 V bias voltage was shown in Figure 11a. The full cycles transient plots are presented in Figure S2 of the Supporting Information. Formal et al.[32] reports that the reaction time scale of water splitting is at ca. 0.5 s^{-1}, assigned to water splitting and assumed constant with bias potential, and the other in the 100−1 s^{-1} range, related to slow recombination on the surface with charge transportations and back electron recombination. When the radiation was in the "on" state, the electric current rises quickly in the I regime. Then, the electric current went down to the steady state current in the II regime. When the radiation was in the "off" state, the negative current is created quickly in the III regime. Then, the electric current rises to another steady state current as the electric current in the dark field. The above transient photoelectric responses refer to the presentation of Figure 11b. In the I regime, the electron−

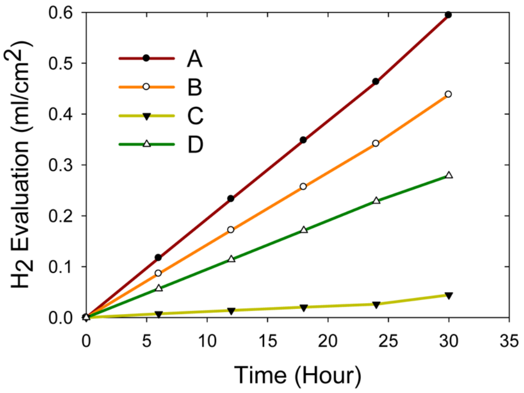

Figure 12. Hydrogen generation evaluation plot of multi-shaped Cu_2O nanoparticles on MnO−MnO_2 nanorods supported by few-layer graphene on an ITO glass substrate as the photocathode with 0.1 M $KHCO_3$ as the electrolyte at 0.6 V bias voltage (A, truncated cubic; B, cuboctahedral; C, truncated octahedral; D, octahedral).

hole pair of Cu_2O generates the electron transport to reduce protons into hydrogen gas, and the electronic hole hops to the valence band of MnO_2 and few-layer graphene in the 100−1 s^{-1} range, which contributes to the rising photocurrent. Then, the electron−hole pair of Cu_2O continues to be generated. The electronic hole and excited electron hop to the valence band of few-layer graphene and reduce hydrogen gas, respectively, in the photocurrent steady state (regime II). Then, the light was in "off" state. Because the reaction time scale of water splitting (ca. 0.5 s^{-1}) is slower than that of back electron recombination (ca. 100−1 s^{-1}), the excited electron hops to the valence band of MnO_2, which contributes to a negative current in the regime III.

The chemical potential of the reaction, $Cu_2O + 2e^- + H_2O \rightarrow 2Cu + 2OH^-$ (0.360 eV vs the reference potential, 0 eV)[33] is higher than that of the hydrogen generation reaction of $2H^+ + 2e^- \rightarrow H_2$ (the reference potential, 0 eV). The hydrogen generation reaction prefers to work in the photocathode in electrochemistry. The Cu_2O in the photocathode after function under photocatalytic conditions was also determined by X-ray diffraction. Cu_2O is not self-reduction into Cu in photocathode. On the other hand, the gas formed in the photocathode was checked by gas chromatography. The formed gas is the hydrogen gas. A hydrogen generation evaluation plot of multi-shaped Cu_2O nanoparticles on MnO−MnO_2 nanorods supported by few-layer graphene on an ITO glass substrate as the photocathode with 0.1 M $KHCO_3$ as the electrolyte at bias voltage 0.6 V is presented in Figure 12. Hydrogen generation evaluations were fit and presented in Table 2. *R* is the hydrogen generation rate. The generated gas is collected by water displacement and determined by gas chromatography. The hydrogenation rate of truncated cubic Cu_2O on MnO−MnO_2 nanorods is 33.0 mL/min m^2 (0.55 mL/sec m^2). The gas generation rate in the photocathode was checked by gas chromatography. According to faradaic efficiency combined with the gas generation rate, the most of the electric currents (A, 77.0%; B, 77.0%; C, 65.1%; D, 77.1%) are utilized to yield hydrogen gas.

According to XRD data in Figure 6, the prefered orientation of the truncated cubic and cuboctahedral Cu_2O nanocrystals is (200). The prefered orientation of the truncated octahedral and octahedral Cu_2O nanocrystals is (111). The propagation of the electronic wave function along (200) is faster than that along (111) because the band structure of Cu_2O in the (111) direction is more flat than that in the (200) direction.[34] Therefore, electronic transportation in the (200) direction is faster that in the (111) for Cu_2O. The truncated cubic and cuboctahedral Cu_2O nanocrystals are higher than the others. The average particle size of the truncated cubic cuboctahedral Cu_2O nanocrystal is larger than that of cuboctahedral Cu_2O nanocrystal, as shown in Table 1. The smaller the particle is, the larger the reaction area of all particles is. According to the APCE data in Figure 10, absorbed photon-to-current conversion efficiency of the truncated cubic Cu_2O nanocrystal is the highest of all others. The excited electron of the truncated cubic Cu_2O nanocrystal transfers into the photocurrent more effectively. According to the transient plot in Figure 11a, the photoelectric response of the truncated cubic Cu_2O nanocrystal is also higher than others. We found that a nanostructure Cu_2O combined with a MnO−MnO_2 nanorod has potential applications in the field of solar hydrogen production in the near future.

■ CONCLUSION

A multi-shaped Cu_2O nanoparticles/MnO−MnO_2 nanorods heterojunction on a few-layer graphene-based electrode serves as the photocathode. Multi-shaped Cu_2O nanoparticles, including truncated cubic shape, cuboctahedral shape, truncated octahedral shape, and octahedral shape, were then coated on the square manganese nanorods as the photosensitizer. When Cu_2O is octahedral-shaped, the best absorption happens at 800 nm. The photoelectrochemical properties of multi-shaped Cu_2O on MnO−MnO_2 nanorods supported by few-layer graphene on an ITO glass substrate were measured with an electrolyte of 0.1 M $KHCO_3$ under AM 1.5 G radiation, and the highest rate of hydrogen generation is 33.0 mL/min m^2 for solar hydrogen generation. The achieved results offer very useful guidelines in designing photocathodes for high-efficiency, low-cost, and flexible photoelectrochemical cells by using cheap, earth-abundant materials for clean solar hydrogen generation at large scales. This study highlights the significance of a back electron−hole recombination loss and transportation process on the surface of a water-splitting photocathode, retarding the appearance of the photocurrent and requiring a greater amount of energy from a solar device.

■ ASSOCIATED CONTENT

Ⓢ Supporting Information

Photoelectric current in dark field and transient plots of multi-shaped Cu_2O nanoparticles on MnO nanorods supported by a graphene layer on an ITO glass substrate as the photocathode. The Supporting Information is available free of charge on the ACS Publications website at DOI: 10.1021/acssuschemeng.5b00579.

■ AUTHOR INFORMATION

Corresponding Author

*Tel: +886-6-2757575, ext 62941. Fax: +886-6-2005437. E-mail: yhsu@mail.ncku.edu.tw.

Notes

The authors declare no competing financial interest.

■ ACKNOWLEDGMENTS

We gratefully acknowledge the Ministry of Science and Technology in Taiwan for financial support in research plan

No. 102-2221-E-006-293 -MY3, 104-2622-E-006-028-CC3, and 103-2622-E-006-040-CC2.

■ REFERENCES

(1) Geim, A. K.; Novoselov, K. S. The rise of graphene. *Nat. Mater.* **2007**, *6*, 183−191.

(2) Stratakis, E.; Stylianakis, M. M.; Koudoumasa, E.; Kymakis, E. Plasmonic organic photovoltaic devices with graphene based buffer layers for stability and efficiency enhancement. *Nanoscale* **2013**, *5*, 4144−4150.

(3) Li, J.; Ren, Z.; Zhou, Y.; Wu, X.; Xu, X.; Qi, M.; Li, W.; Bai, J.; Wang, L. Scalable synthesis of pyrrolic N-doped graphene by atmospheric pressure chemical vapor deposition and its terahertz response. *Carbon* **2013**, *62*, 330.

(4) Kuzmenko, A. B.; van Heumen, E.; Carbone, F.; van der Marel, D. Universal infrared conductance of graphite. *Phys. Rev. Lett.* **2008**, *100*, 117401.

(5) Paton, K. R.; Varrla, E.; Backes, C.; Smith, R. J.; Khan, U.r; O'Neill, A.; Boland, C.; Lotya, M.; Istrate, O. M.; King, P.; Higgins, T.; Barwich, S.; May, P.; Puczkarski, P.; Ahmed, I.; Moebius, M.; Pettersson, H.; Long, E.; Coelho, J.; O'Brien, S. E.; McGuire, E. K.; Sanchez, B. M.; Duesberg, G. S.; McEvoy, N.; Pennycook, T. J.; Downing, C.; Crossley, A.; Nicolosi, V.; Coleman, J. N. Scalable production of large quantities of defect-free few-layer graphene by shear exfoliation in liquids. *Nat. Mater.* **2014**, *13*, 624−630.

(6) Brock, S. L.; Duan, N.; Tian, Z. R.; Giraldo, O.; Zhou, H.; Suib, S. L. A review of porous manganese oxide materials. *Chem. Mater.* **1998**, *10*, 2619−2628.

(7) Wang, N.; Pang, H.; Peng, H.; Li, G.; Chen, X. Hydrothermal synthesis and electrochemical properties of MnO_2 nanostructures. *Cryst. Res. Technol.* **2009**, *44*, 1230−1234.

(8) Siriwong, C.; Phanichphant, S. Flame-made single phase Zn_2TiO_4 nanoparticles. *Mater. Lett.* **2011**, *65*, 2007−2009.

(9) Chen, Y.; Zhang, Y.; Geng, D.; Li, R.; Hong, H.; Chen, J.; Sun, X. One-pot synthesis of MnO_2/graphene/carbon nanotube hybrid by chemical method. *Carbon* **2011**, *49*, 4434−4442.

(10) Cheng, Q.; Tang, J.; Ma, J.; Zhang, H.; Shinya, N.; Qin, L.-C. Graphene and nanostructured MnO_2 composite electrodes for supercapacitors. *Carbon* **2011**, *49*, 2917−2925.

(11) Wu, Z.-S.; Ren, W.; Xu, L.; Li, F.; Cheng, H.-M. Doped graphene sheets as anode materials with superhigh rate and large capacity for lithium ion batteries. *ACS Nano* **2011**, *5*, 5463−5471.

(12) Fan, Z.; Yan, J.; Wei, T.; Zhi, L.; Ning, G.; Li, T.; Wei, F. Asymmetric Supercapacitors Based on Graphene/MnO_2 and Activated Carbon Nanofiber Electrodes with High Power and Energy Density. *Adv. Funct. Mater.* **2011**, *21*, 2366−2375.

(13) Hall, P. J.; Mirzaeian, M.; Fletcher, S. I.; Sillars, F. B.; Rennie, A. J. R.; Shitta-Bey, G. O.; Wilson, G.; Cruden, A.; Carter, R. Energy storage in electrochemical capacitors: designing functional materials to improve performance. *Energy Environ. Sci.* **2010**, *3*, 1238−1251.

(14) Chen, P.-C.; Shen, G.; Shi, Y.; Chen, H.; Zhou, C. Preparation and characterization of flexible asymmetric supercapacitors based on transition-metal-oxide nanowire/single-walled carbon nanotube hybrid thin-film electrodes. *ACS Nano* **2010**, *4*, 4403−4411.

(15) Kudo, A.; Miseki, Y. Heterogeneous photocatalyst materials for water splitting. *Chem. Soc. Rev.* **2009**, *38*, 253.

(16) Abe, R. Recent progress on photocatalytic and photoelectrochemical water splitting under visible light irradiation. *J. Photochem. Photobiol., C* **2010**, *11*, 179−209.

(17) Baldea, I.; Köppel, H.; Cederbaum, L. S. Characterization of assembled quantum dots and single−electron transistors by photoemission and photoabsorption. *Phys. Stat. Solidi C* **2010**, *7*, 2671.

(18) Chen, H.; Ratner, M. A.; Schatz, G. C. Time-dependent theory of the rate of photo-induced electron transfer. *J. Phys. Chem. C* **2011**, *115*, 18810−21.

(19) Ng, C. H. B.; Fan, W. Y. Shape Evolution of Cu_2O Nanostructures via Kinetic and Thermodynamic Controlled Growth. *J. Phys. Chem. B* **2006**, *110*, 20801.

(20) Hara, M.; Kondo, T.; Komoda, M.; Ikeda, S.; Shinohara, K.; Tanaka, A.; Kondo, J. N.; Domen, K. Cu2O as a photocatalyst for overall water splitting under visible light irradiation. *Chem. Commun.* **1998**, *4*, 357−358.

(21) Xu, H.; Wang, W.; Zhu, W. Shape evolution and size-controllable synthesis of Cu2O octahedra and their morphology-dependent photocatalytic properties. *J. Phys. Chem. B* **2006**, *110*, 13829.

(22) Konios, D.; Stylianakis, M. M.; Stratakis, E.; Kymakis, E. Dispersion behaviour of graphene oxide and reduced graphene oxide. *J. Colloid Interface Sci.* **2014**, *430*, 108−112.

(23) O'Neill, A.; Khan, U.; Nirmalraj, P. N.; Boland, J.; Coleman, J. N. Graphene Dispersion and Exfoliation in Low Boiling Point Solvents. *J. Phys. Chem. C* **2011**, *115*, 5422−5428.

(24) Rao, C. N. R.; Sood, A. K.; Subrahmanyam, K. S.; Govindaraj, A. Graphene: the new two-dimensional nanomaterial. *Angew. Chem., Int. Ed.* **2009**, *48*, 7752.

(25) Stratakis, E.; Eda, G.; Yamaguchi, H.; Kymakis, E.; Fotakis, C.; Chhowalla, M. Free-standing graphene on microstructured silicon vertices for enhanced field emission properties. *Nanoscale* **2012**, *4*, 3069−3074.

(26) Park, H. J.; Meyer, J.; Roth, S.; Skákalová, V. Growth and properties of few-layer graphene prepared by chemical vapor deposition. *Carbon* **2010**, *48*, 1088−1094.

(27) Malard, L. M.; Pimenta, M. A.; Dresselhaus, G.; Dresselhaus, M. S. Raman spectroscopy in graphene. *Phys. Rep.* **2009**, *473*, 51−87.

(28) McShane, C. M.; Choi, K.-S. Junction studies on electrochemically fabricated p−n Cu2O homojunction solar cells for efficiency enhancement. *Phys. Chem. Chem. Phys.* **2012**, *14*, 6112−6118.

(29) Isseroff, L. Y.; Carter, E. A. Electronic Structure of Pure and Doped Cuprous Oxide with Copper Vacancies: Suppression of Trap States. *Chem. Mater.* **2013**, *25*, 253−265.

(30) Zhou, H.; Wu, L.; Gao, Y.; Ma, T. Dye-sensitized solar cells using 20 natural dyes as sensitizers. *J. Photochem. Photobiol., A* **2011**, *219*, 188−194.

(31) So, P. T. C.; Dong, C. Y.; Masters, B. R.; Berland, K. M. Two-phton excitation fluorescence microscopy. *Annu. Rev. Biomed. Eng.* **2000**, *2*, 399−429.

(32) Le Formal, F.; Pendlebury, S. R.; Cornuz, M.; Tilley, S. D.; Grätzel, M.; Durrant, J. R. *J. Am. Chem. Soc.* **2014**, *136*, 2564−2574.

(33) Haynes, W.M. *Handbook of Chemistry and Physics*, 93rd ed., Chemical Rubber Company, 2012; pp 5−80; ISBN 9781439880494.

(34) Heinemann, M.; Eifert, B.; Heiliger, C. Band structure and phase stability of the copper oxides Cu_2O, CuO, and Cu_4O_3. *Phys. Rev. B: Condens. Matter Mater. Phys.* **2013**, *87*, 115111.